PAPER

Passive scalar transport mediated by laminar vortex rings

IOP Publishing | The Japan Society of Fluid Mechanics Fluid *Dynamics* Research

Fluid Dyn. Res. **49** (2017) 025514 (21pp) https://doi.org/10.1088/1873-7005/aa5b59

Passive scalar transport mediated by laminar vortex rings

R H Hernández and G Rodríguez

LEAF-NL, Depto. Ingeniería Civil Mecánica, Universidad de Chile, Casilla 2777, Santiago, Chile

E-mail: rohernan@ing.uchile.cl

Received 14 April 2016, revised 17 December 2016
Accepted for publication 20 December 2016
Published 28 February 2017

Communicated by Anne Juel

Abstract

Numerical simulations were used to study the dynamics of a passive conserved scalar quantity entrained by a self-propelling viscous vortex ring. The transport and mixing process of the passive scalar variable were studied considering two initial scalar distributions: (i) The scalar substance was introduced into the ring during its formation, further focusing in the shedding into the wake of the ring; (ii) A disk-like scalar layer was placed in the ring's path where the entrainment of the scalar substance into the ring bubble was studied as a function of the ring strength. In both cases, the scalar concentration inside the vortex bubble exhibits a steady decay with time. In the second case, it was shown that the entrained scalar mass grows with both the Reynolds number of the ring and the thickness of the scalar layer in the propagation direction. The ring can be viewed as a mechanism for scalar transportation along important distances.

Keywords: vortex rings, vorticity, passive scalar transport, numerical simulations

(Some figures may appear in colour only in the online journal)

1. Introduction

The objective of this work is to determine the ability of stable and laminar vortex rings to transport a scalar substance across a viscous fluid originally at rest. The substance behaves as a scalar whose concentration is governed by both fluid advection and molecular diffusion relative to the fluid, and it is conserved because it is neither produced nor destroyed in the flow. Moreover, it is a passive scalar having no direct influence on the background flow. The

choice of a vortex ring to promote scalar transport and mixing provides a well-documented symmetric flow field in permanent motion which allows for a simple theoretical frame to understand the scalar dynamics. The interest in the structures of vortex rings originated from the pioneering works of Hicks and Kelvin in the 19th century (Kelvin 1867, 1881, Hicks 1885). Laminar vortex rings have not only been considered a fundamental example of canonical flows in vorticity and scalar dynamics (Southerland *et al* 1991) but are also viewed as coherent structures in fluid mechanics (Roberts and Donelly 1970) described by compact distributions of vorticity allocated into what we call the core of the ring (Lamb 1932, Saffman 1970).

Interesting ring dynamics results from the self-propagating ability of such vortex structures, easy to create and highly reproducible in the laboratory, when working in the stable regime at low Reynolds numbers $Re < 600$ (where Re is based on ring velocity and ring diameter) (Widnall and Sullivan 1973, Chatelain *et al* 2003). In nature we find examples of vortex ring formation in phenomena ranging from volcanic fumes to the mechanisms of propulsion of marine organisms (Linden and Turner 2001). At the laboratory scale (Maxworthy 1972, 1977) rings are created by discharging fluid slug through either a circular orifice or a nozzle (Gharib *et al* 1998, Glezer 1988, Glezer and Coles 1990).

There exist a large amount of bibliography records and research papers on vortex rings (see for instance the review of (Shariff and Leonard 1992)), however the mechanisms involved in the scalar entrainment of laminar rings appear to be much less documented. The velocity field associated to a ring can produce an important entrainment of a given scalar substance present in the fluid (Muller and Didden 1980). The determination of the entrainment fraction is one of the goals of this kind of study, showing that entrainment fractions of 30–40% can be reached depending on the stroke ratio used to create rings (Dabiri and Gharib 2004). Being particularly difficult to resolve the fluid entrainment during the vortex ring formation in an experiment, some numerical studies have examined entrainment by vortex rings in small (James and Madnia 1995) and high (Southerland *et al* 1991) stroke ratios typically with uniform scalar distributions in the vortex ring generator. The relative success of vortex rings to trap scalars motivated very interesting works on the interaction between rings and particles. Small particle distributions located in the vortex ring path may be trapped by the ring and then conveyed over long distances (Uchiyama and Yagami 2008, 2009).

In this study we adopt a slightly different approach to introducing both the scalar quantity and create the vortex rings in order to evaluate the mixing and scalar transport. Self-propelling vortex rings are created modelling, as close as possible, a real experiment using a circular nozzle and a smooth and more realistic s-shaped piston displacement profile specified at the generating chamber of the system. At some distance from the chamber exit, the rings will cross a disk-like scalar layer placed in the ring's path to determine the effect of the ring properties on the entrainment process.

2. Formulation

How do we create a ring? Most numerical simulations on vortex rings dynamics usually start either with the Dirichlet boundary condition at the nozzle section imposing an uniform velocity profile (Sau and Mahesh 2007) or with an initial velocity field computed from the Biot–Savart analogy for vortex filaments (Chatelain *et al* 2003, Uchiyama and Yagami 2009) considering typically a Gaussian vorticity distribution at the vortex core.

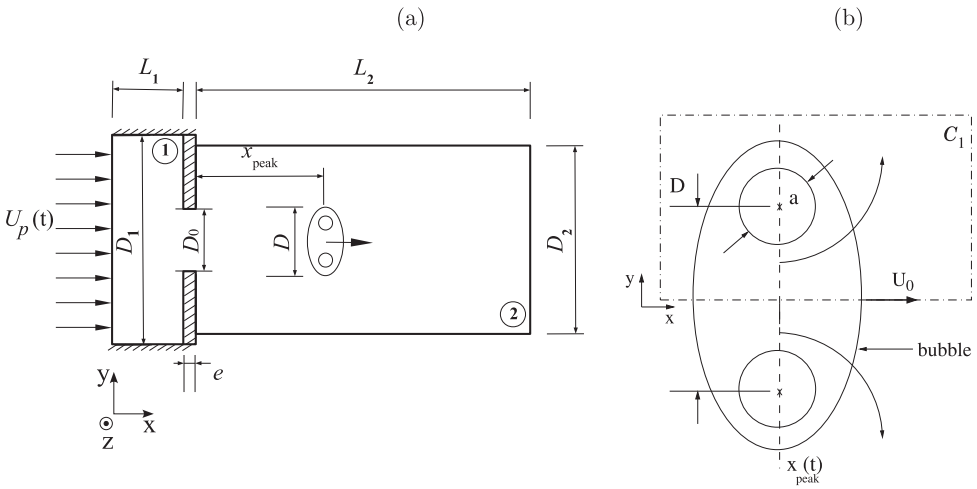

Figure 1. (a) Scheme of the tridimensional domain showing the piston and generation chamber of diameter D_1, the nozzle diameter D_0 and free boundaries's domain of length L_2 where the vortex ring develops and moves freely. The dimensions are $D_1 = 100$, $D_2 = 80$, $D_0 = 15$, $L_1 = 20$, $L_2 = 160$ and $e = 1.5$ (mm). (b) Schematics of a middle plane symmetric vortex ring in free flight. We indicate the position of the ring $x_{\text{peak}}(t)$ referred to the nozzle in chamber (1) and the main length scales of the ring, like overall diameter D, core diameter a and self-induced velocity U_0.

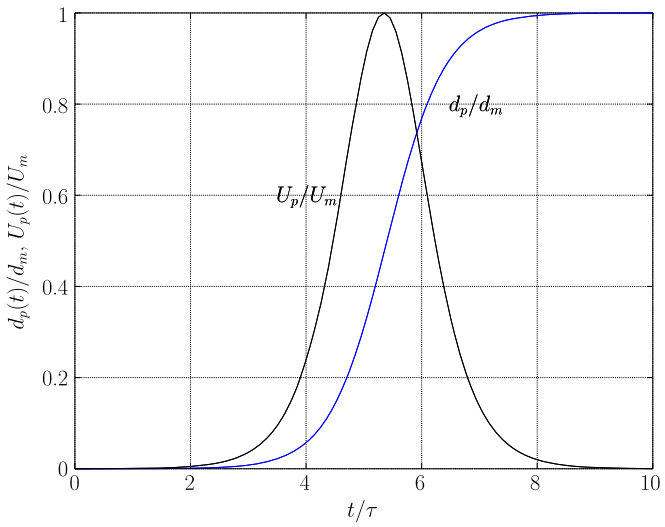

Figure 2. S-shaped forcing signal $d_p(t)$ representing the normalised piston position in time inside the chamber. We also display the resulting piston velocity $U_p(t)$ normalised by its maximum value U_m.

In this work we will adopt a more realistic vortex generation; we will obtain the velocity and pressure conditions at the nozzle from the simulation of an upstream chamber where a flat piston motion is modelled as shown in figure 1.

The fluid in the chamber, at rest and incompressible, is pushed rapidly by a flat piston motion defined by a particular s-shaped piston displacement profile (see figure 2), giving life to axisymmetric vorticity sheets created at the chamber walls and borders, that roll up at the exit hole of the nozzle, producing a self-propelling vortex ring. Typical dimensions of a ring are shown in figure 1, where we also display the diametral plane of a ring indicating schematically the ring diameter D, vortex core size a and self-induced velocity U_0. In order to validate the numerical simulation we have tried to reproduce laboratory conditions, adopting here a geometry similar to experimental devices used in previous studies (Arévalo *et al* 2007, Astudillo 2008). The geometry and dimensions of the computational domain are shown in figure 1. There is a cylindrical chamber (1) of diameter D_1 and length L_1 forced by a flat piston at the left of the figure which has a circular nozzle of diameter D_0 at the right end which discharges a fluid mass into the open cylindrical domain (2) of diameter D_2 and length L_2. There is considerable information about the right choice of the ratio D_0/L_2 in the literature. According to previous studies (James and Madnia 1995, Sau and Mahesh 2007), the discharge domain (2) should have a diameter between six and eight times the diameter of the nozzle while a length $L_2 \sim 10D_0$ allows for enough space to track the three fundamental stages in the development of the ring (Southerland *et al* 1991).

The numerical simulation solves the mass conservation equation, incompressible Navier–Stokes and scalar concentration equations in primitive variables

$$\nabla \cdot \vec{V} = 0 \tag{1}$$

$$\frac{\partial \vec{V}}{\partial t} + (\vec{V} \cdot \nabla)\vec{V} = -\frac{1}{\rho}\nabla p + \nu \nabla^2 \vec{V} \tag{2}$$

$$\frac{\partial C}{\partial t} + (\vec{V} \cdot \nabla)C = \Gamma_c \nabla^2 C \tag{3}$$

where $\vec{V} = (u, v, w)$ is the vector velocity, p is the pressure, ν the kinematic viscosity, ρ is the density, $C(\vec{x}, t)$ is the scalar concentration and Γ_c is the scalar diffusivity.

Boundary conditions for the simulation are Neumann conditions for the velocity and atmospheric pressure conditions at the discharge domain (2) in figure 1. On lateral walls we imposed no-slip condition for all velocity components. The initial concentration of the scalar can be set to any value between $0 \leqslant C \leqslant 1$ in any place of the physical domain. In this work we will consider two initial conditions for the scalar concentration in relation to the ring motion. In the first case the scalar concentration is set to $C = C_0$ distributed in the border of the nozzle to try to inject scalar into a forming ring to account for the scalar fraction trapped inside the ring.

The second case is a disk-like scalar layer of thickness ϵ and diameter $D_\epsilon > D_0$, where the scalar concentration is set to a given value $C = C_0$ as the initial condition. The idea is to place a scalar layer in the ring path and force the interaction when the ring crosses it, finally accounting for the scalar mass fraction trapped by the ring. In both situations, the rest of the domain is set to $C = 0$.

The boundary conditions in the chamber are

$$\begin{aligned} x = -L_1,\ |r| \leqslant \tfrac{D_1}{2} \qquad & \rightarrow u_x = u_p(t),\ u_y = u_z = 0 \\ \begin{pmatrix} -L_1 \leqslant x \leqslant -e, & |r| = \tfrac{D_1}{2} \\ x = -e, & \tfrac{D_0}{2} \leqslant |r| \leqslant \tfrac{D_1}{2} \\ -e \leqslant x \leqslant 0, & |r| = \tfrac{D_1}{2} \end{pmatrix} & \rightarrow \quad u_x = u_y = u_z = 0 \end{aligned} \tag{4}$$

where $r = \sqrt{y^2 + z^2}$. The boundary conditions in the discharge domain are

$$\begin{aligned} x = 0,\ \tfrac{D_0}{2} \leqslant |r| \leqslant \tfrac{D_2}{2} \quad & \rightarrow u_x = u_y = u_z = 0 \\ \begin{pmatrix} 0 < x \leqslant L_2, & |r| = \tfrac{D_2}{2} \\ x = L_2, & |r| \leqslant \tfrac{D_2}{2} \end{pmatrix} & \rightarrow \tfrac{\partial u_x}{\partial x} = 0,\ \tfrac{\partial u_y}{\partial x} = 0 \end{aligned} \tag{5}$$

Detailed boundary conditions for the each scalar case will be discussed in section 3.2.

Based on previous works (James and Madnia 1995, Mohseni *et al* 2001, Hernández *et al* 2006) the piston motion defined by $d_p(t)$ can be modelled as a hyperbolic function given in equation (6),

$$d_p(t) = \frac{d_0}{2}\left[1 + \tanh\left(\frac{t - t_0}{\tau}\right)\right] \tag{6}$$

Here t_0 represents a time lag for piston motion, τ is the characteristic time of the function and d_0 is the maximum piston displacement or piston stroke. The piston velocity is found as the time derivative of the piston position, $U_p(t) = \dot{d}_p(t)$ which has the shape shown in figure 2. The characteristic time τ of the piston motion is imposed in the forcing function $d_p(t)$ given by equation (6), in the same way as it was obtained from the experimental settings of a piston-based vortex generator in Arévalo *et al* (2007). Given that the hyperbolic tangent function never reaches zero values, the time origin $t = 0$ for the piston's displacement in the simulation was defined as the instant when the piston velocity is maximum ($t = t_0$). This time reference provides an alternative option to compute the self-induced velocity of the ring based on its position in the x-axis and flight time by means of a continuous tracking of peak velocity along the ring's path.

2.1. Numerical method

The equations were solved with the software Fluent version 6.3 (FLUENT INC., 2005) using the built-in control volume formulation under the SIMPLEC algorithm (Patankar 1980).

Simulations were performed on a 8 CPU Dell Precision T5500 workstation cluster running Open Suse Linux and based on MPI libraries. The CPU run time for one ring to propagate across the entire domain was about 20 hours. According to Jang *et al* (1986) the algorithm exhibits a better behaviour than other methods when convergence in small time steps is required. The geometry of the vortex generator required a fine spatial discretisation, particularly in zones of high velocity gradients such as the nozzle walls. Similarly, as a result of the rapid ring formation and subsequent motion, the temporal discretisation required time steps under 5 (ms), thus we choose a time step size $\Delta t = 1$ ms for all the simulations.

A set of grid tests were performed to look for grid independent results. We performed grid tests with radially varying mesh grids using approximation functions to be able to vary the grid size in regions where the shear stresses during ring formation can be high, like at the

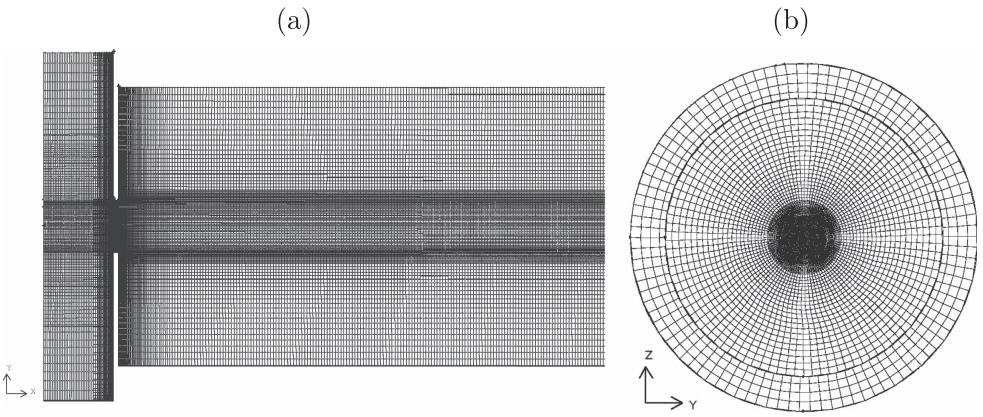

Figure 3. Midplane and cross section slices of the mesh grid used. Grid size decreases in regions like the chamber walls close to the nozzle and along the central region of the downstream section where the ring moves.

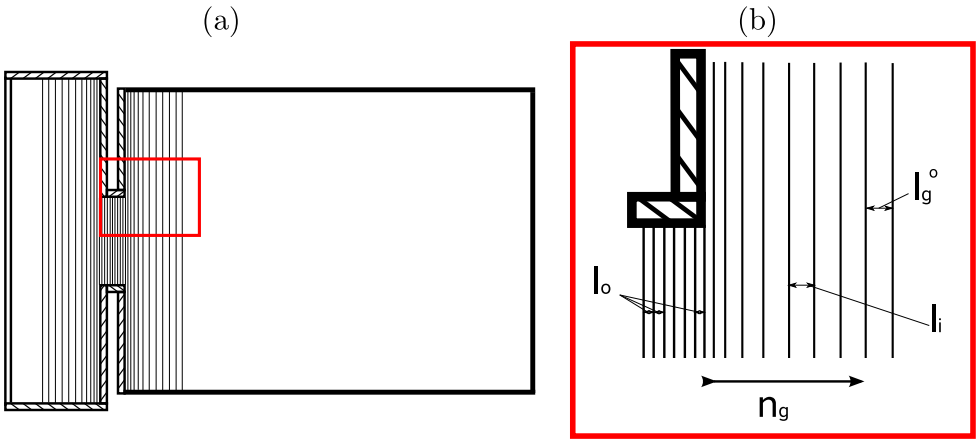

Figure 4. Longitudinal mesh grid schematics (a) close to the nozzle. (b) Zoom of the grid size progression in the axial direction.

vicinity of the exit nozzle of the vortex generator (see table 1). The element size inside the nozzle (width e) is l_0 and constitutes the basic scale to build up the rest of the longitudinal elements of both the left chamber making the piston stroke and the right-side domain, respectively. These preliminary tests with different grids allowed for an appropriate choice of the mesh size without compromising accuracy and CPU time (cf figure 3). However we also required the resulting velocity profiles and ring properties to match as closely as possible to the experimental results from the work of Arévalo *et al* (2007).

The spatial discretisation of the geometry can be observed in figure 4 where we show the longitudinal mesh based on rectangular elements. In order to maintain the grid size within reasonable limits, the longitudinal mesh in both chambers or domains involves an approximation function where the longitudinal element size l_i is computed with the following geometric law, $l_i = l_0 r^{(i-1)} \ \forall \ i < n_j$, where r is the geometric growth rate. After n_j the

Table 1. Grid sizes. The element size inside the nozzle is l_0.

Grid	N° of elements	Domain length (L_2/D_o)	Element size (e/l_o)
Coarse-1	2×10^5	6	4.2
Coarse-2	7×10^5	6	4.2
Coarse-3	8.5×10^5	10	15
Fine-1	1.4×10^6	6	4.2
Fine-2	1.6×10^6	10	15

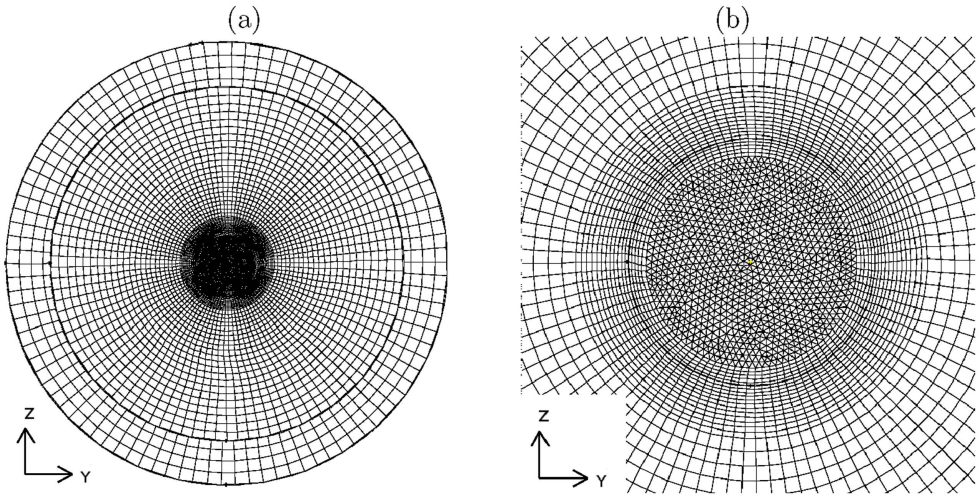

Figure 5. (a) Fine-2 grid in the y-z plane. (b) Zoom of the center of the Fine-2 grid with triangular elements.

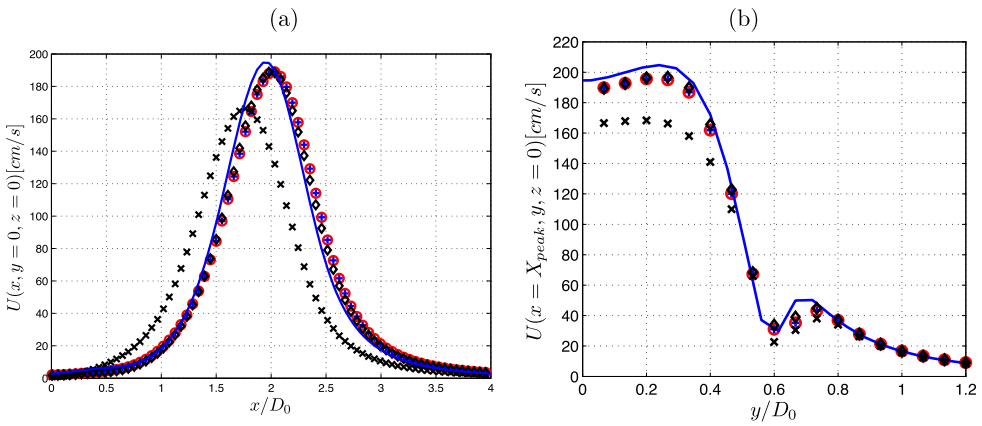

Figure 6. Comparison of (a) axial velocity profiles and (b) transverse velocity profiles at $X_{\text{peak}} = 2D_0$ for different grids: Coarse-1 grid (×) , Coarse-2 grid (○), Coarse-3 grid (+), Fine-1 grid (◊), Fine-2 grid (-).

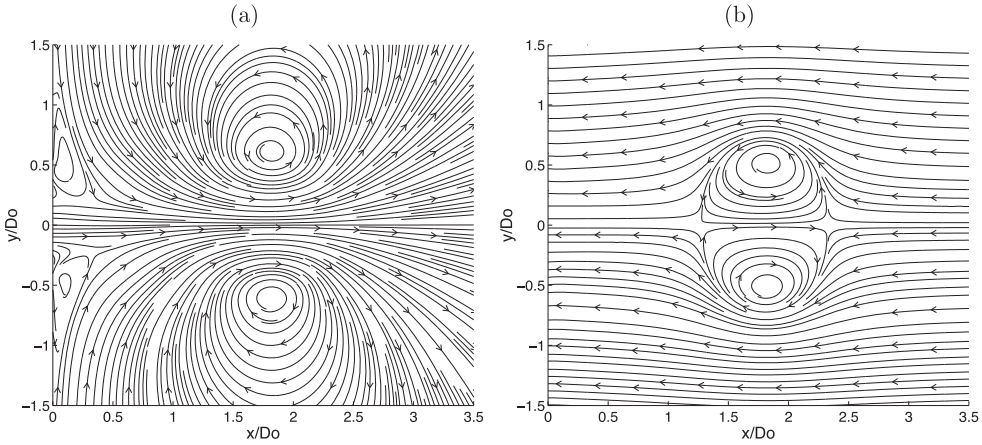

Figure 7. (a) Instantaneous streamlines in the laboratory frame of reference. (b) Instantaneous streamlines in the reference frame moving with the vortex ring where we clearly observe the vortex ring bubble. The position has been normalised with the nozzle diameter D_0.

elements maintain a constant size lg^{o} in the vortex generator and le^{o} in the developing zone of the ring.

Figure 5 shows the coarse grid in the *x*-*y* plane combined with a centre grid refinement based upon triangular elements which provided reasonable agreement with the experimental results and at the same time give us grid independent results as shown in figure 6.

Results from the grid tests are shown in figure 6 where the rings share the same initial and boundary conditions. The axial position of the velocity maximum indicates how rapid the vortex ring is for a given time. Looking at the maximum of the velocity versus the *x* plot, we see that the coarse grid had a strong effect producing slow rings when compared with finer grids. In this work we have chosen the fine-2 grid because the characteristic properties of the rings are close to both the numerical results of (Astudillo 2008) and to the recent experimental results of (Hernández and Monsalve 2015).

In figure 6 the comparison of the numerical and experimental data shows a better agreement in the case of fine grids both in the case of axial velocity and transverse velocity profiles.

Properties of the fluid used in this study are given in table 2 (CRC 2009). Carbon monoxide was chosen as a passive scalar with its density and viscosity relatively similar to those of air under similar atmospheric conditions. Our interest was to study the ability of vortex rings to transport such a toxic gas from one production site to a different site electing rings as candidates to clean up a determined atmosphere contaminated with CO.

According to the given properties, the Schmidt number of the mixture is defined as $S_c = \nu/\Gamma_c = 0.54$ which corresponds to an important diffusive effect. If the diffusivity of the solute in the solvent is low and the kinematic viscosity (ν) is high, then the Schmidt number is high and the solute dynamics makes mixing very difficult under laminar flow conditions. Therefore, when the Schmidt number is small, $Sc < 1$, both substances will tend to mix easily due to a dominant diffusive effect. Under this condition the numerical simulations will test the interesting transport properties of vortex rings, since *a priori* there will be a high tendency to mix between the two substances. The case of higher Schmidt numbers has been well-

Table 2. Fluid properties.

Fluid	ρ (kg/m^3)	ν (m^2/s)	Γ_c (m^2/s)
Air	1.225	1.7894×10^{-5}	
Carbon monoxide	1.1233	1.7500×10^{-5}	2.88×10^{-5}

documented in the literature to understand the mixing properties associated with vortex rings (Southerland *et al* 1991, Sau and Mahesh 2007).

2.2. Vortex ring properties

An interesting parameter of the ring is the bubble or Kelvin oval (Southerland *et al* 1991) associated with the ring. This oval is like an envelope acting like a boundary between the flow and the ring during its motion. This oval is defined between the streamlines passing through the front and the rearward stagnation points of the ring (figure 1(b)). As the velocity field of a ring is the combination (non-linear) between its own velocity field created by the vortex ring core and the additional advection flow field observed when it moves across the fluid with a self-induced velocity U_0, we have to compute at each time step the geometry and position of the bubble but in the frame of reference moving with the ring.

Figure 7(a) shows the instantaneous streamlines of a typical ring which were computed directly from the absolute velocity field ($\vec{V} = (u, v, w)$) seen in an inertial frame of reference. Now, if we change into a reference frame moving with the ring at U_0, the velocity field is given by ($\vec{V'} = (u - U_0, v, w)$) and we observe in figure 7(b) the streamlines defining the Kelvin oval or bubble between the rear and front stagnation points. After that we are able to account for the scalar mass trapped inside the bubble at any time after pinch-off.

The ring bubble in figure 7(b) resembles an ellipse (ellipsoid in the 3D) and according to (Dabiri and Gharib 2004) the bubble accepts an ellipsoidal adjustment, where the ellipsoidal focus in a given plane (e.g. x-y) lies in the rotation points of the ring core, and the distance to the minor semi-axis is the distance between the center of the ring and the stagnations point in the frame of reference of the ring. The volume of the ring bubble is then computed using an ellipsoidal fit of the fluid velocity at different locations with respect to the front and rear stagnation points as well as the radial size of the ring (Dabiri and Gharib 2004, Sau and Mahesh 2007).

Now we can calculate the scalar mass trapped inside the ring using the scalar density ρ_s and the volumetric scalar concentration $C(\vec{x}, t)$. The bubble scalar mass can be written as

$$m_b(t) = \int_{\text{bubble}} \rho_s \, C(\vec{x}, t) \, \mathrm{d}x \, \mathrm{d}y \, \mathrm{d}z$$

3. Results

3.1. Vortex ring properties

We performed different numerical runs to measure typical properties of vortex rings in free flight. Results were validated by comparison with experimental data obtained in our laboratory (Arévalo *et al* 2007, 2010) for different values of the Reynolds number, defined as $Re = U_0 D_0 / \nu$. The position of the ring is selected as the position of the maximum velocity,

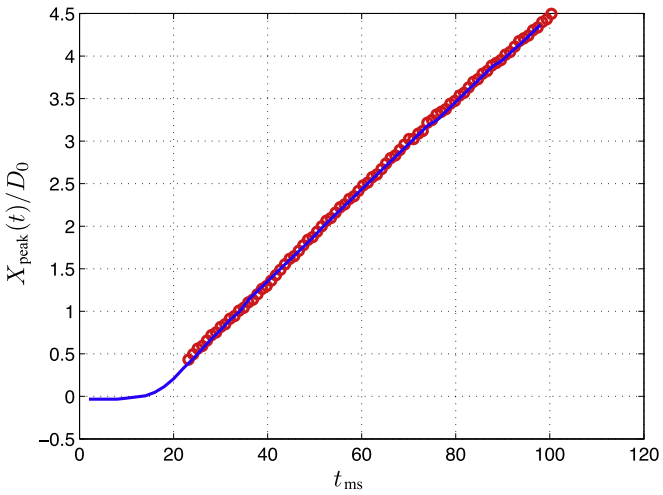

Figure 8. Ring position as a function of time. Comparison of our results (–) with experimental (○) results from Arévalo *et al* (2007) are shown for $Re \sim 700$. The piston stroke is $d_0 = 0.48$ mm and the rise time $\tau = 18.1$ ms.

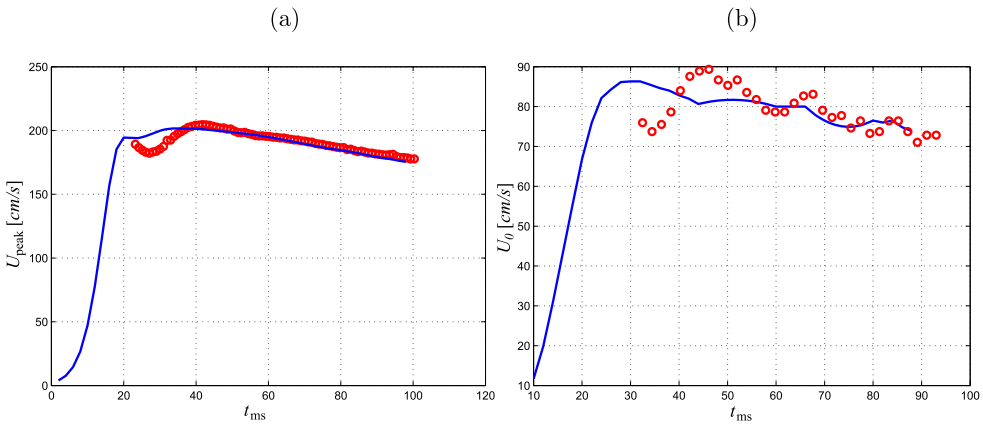

Figure 9. (a) Peak velocity U_{peak} and (b) self-induced velocity U_0 as a function of time. Comparison of our results (–) with experimental (○) results from Arévalo *et al* (2007) are shown for $Re \sim 700$. The piston stroke is $d_0 = 0.48$ mm and the rise time $\tau = 18.1$ ms.

U_{peak}, on the central axis shown in figure 1. Ring velocity U_0 is calculated as the derivative of the position with respect to time.

Figure 8 shows a comparison of the time evolution of ring position, $X_{\text{peak}}(t)$, with similar experimental data, while figure 9 shows the comparison of the maximum axial velocity, U_{peak}, and self-induced velocity, U_0, with THE experimental data of Arévalo *et al* (2007).

Figure 9 shows a comparison of both peak axial velocity $U_{\text{peak}}(t)$ and self-induced velocity $U_0(t)$ with experimental values from Arévalo *et al* (2007) during the post-formation stage of the ring. Good agreement was found with differences below 3% on both curves. The ring velocity is computed with $U_0(t) = dX_{\text{peak}}/dt$ where dt is the time interval between two

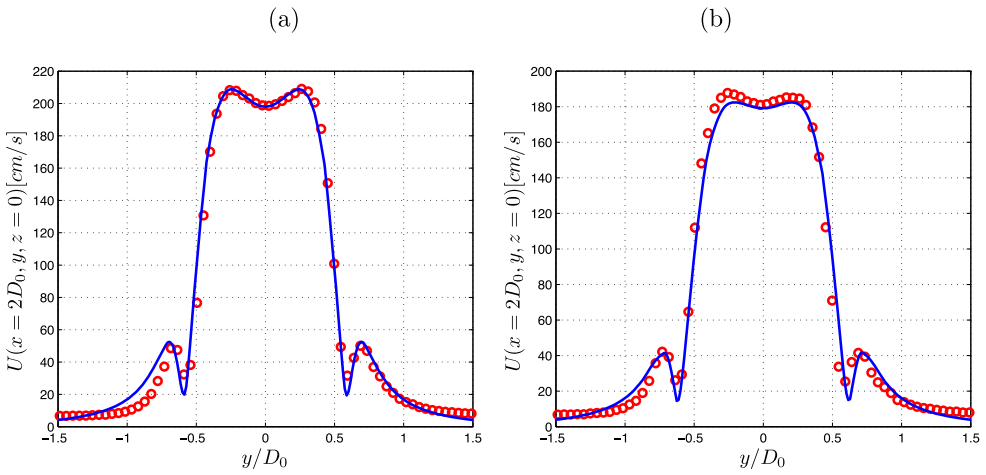

Figure 10. Midplane velocity profile at (a) $X_{\text{peak}} = 2D_0$ and (b) $X_{\text{peak}} = 4D_0$ for numerical (-) and the experimental (○) results of Arévalo *et al* (2007) at $Re \sim 700$.

consecutive X_{peak} values. The related uncertainties in the estimation of the ring velocity come from the accuracy on the determination of the position of peak velocity.

The comparison test was performed between the experimental and simulated rings using a similar ring production mechanism with a rising time of $\tau = 18.1$ ms and same nozzle diameter, which corresponds to a Reynolds number of $Re \sim 700$. In similar works (James and Madnia 1995, Astudillo 2008) the validation of a simulation was based on the comparison of particular velocity profiles in the physical domain.

In figure 10, a comparison between the magnitude of velocity profiles obtained at two downstream axial positions of the ring; $X_{\text{peak}} = 2D_0$ and $X_{\text{peak}} = 4D_0$. The numerical and experimental velocity profiles in figures 10 show a very good agreement in the velocity profile across the transverse coordinate y. There is a 5% relative difference across the high velocity central region.

The velocity profiles in one point of the ring are not enough to claim complete agreement between the experiments and numerical simulations. We need to plot the spatial extension of the velocity field to evaluate the overall differences. In figure 11 we show a qualitative comparison between the spatial velocity fields for the experimental (top) and simulated ring (bottom) using the colour maps of velocity. These results show the small spatial differences associated with the natural fluctuations in the experimental velocity field due to the way the velocity measures were done over each spatial point (Arévalo *et al* 2007). Nevertheless, both the range and spatial similarity are close to within 5% of the main velocity properties of the vortex ring.

A series of numerical runs were performed with rings created with different generation parameters (piston stroke and velocity), in order to understand the effect of the self-induced velocity of the ring on the scalar transport properties.

Vortex rings are created by the action of the piston velocity $U_p(t)$. The higher $U_p(t)$ the higher the ring self-induced velocity $U_0(t)$. As we can see, the S-shaped forcing signal driving the piston displacement $d_p(t)$ inside the chamber (equation (6)) can be varied either by changing the piston stroke d_0 or the characteristic time τ as shown in the next section.

The vortex ring axial position versus time, produced by different generation parameters is shown in figure 12. After some time the curves evolve with time according to the self-induced

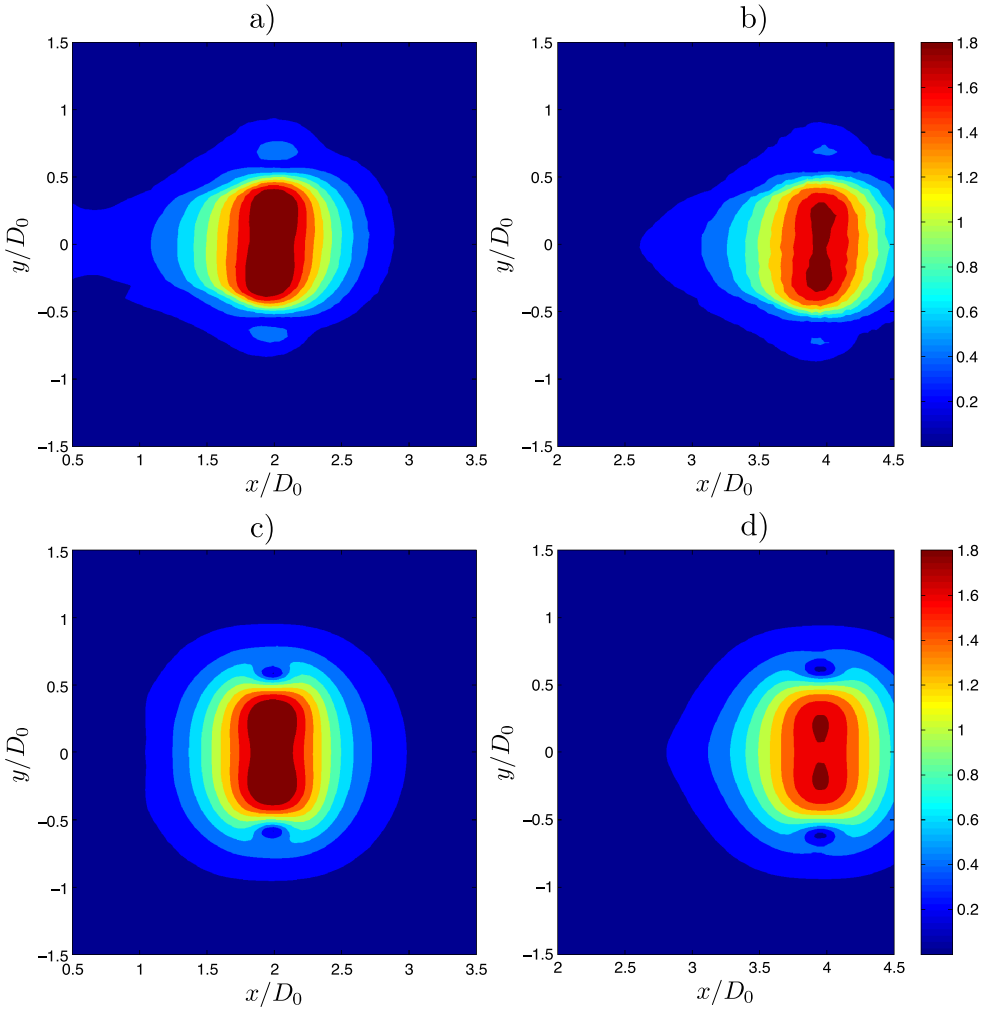

Figure 11. Velocity contours (in m s^{-1}) at positions $X_{\text{peak}} = 2D_0$ and $X_{peak} = 4D_0$ for experimental (a), (b) and simulated (c), (d) rings at Reynolds number $Re = 700$.

velocity U_0 of each ring. We observe that the smaller the rise time the higher the slope of the $X_{peak}(t)$ curve and therefore the ring moves faster. The slope of the curve give us the averaged self-induced velocity of the ring which can be computed by fitting a straight line fit and finding the fit's slope, or, alternatively, we can explicitly compute it as $U_0 = dX_{\text{peak}}(t)/dt$.

The evolution of the axial ring position with time in the case of constant stroke (figure 12(b)) can be collapsed into one single curve when we use the dimensionless time scale $t^* = t/\tau$. However, in the case of varying stroke (figure 12(a)) the time scale normalisation is not enough to produce the collapse as we need to take into account the effect of the stroke in the ring's bubble size (Gharib *et al* 1998).

The self-induced velocity of the ring is directly determined by the piston stroke d_0 or the time scale τ of the forcing signal (figures 12(c), (d)). Once the ring is created, U_0 which is related to vortex core size and ring strength, is observed to decrease as a result of an increase in the ring's diameter and a decrease in strength due to the vorticity shed into the wake of the

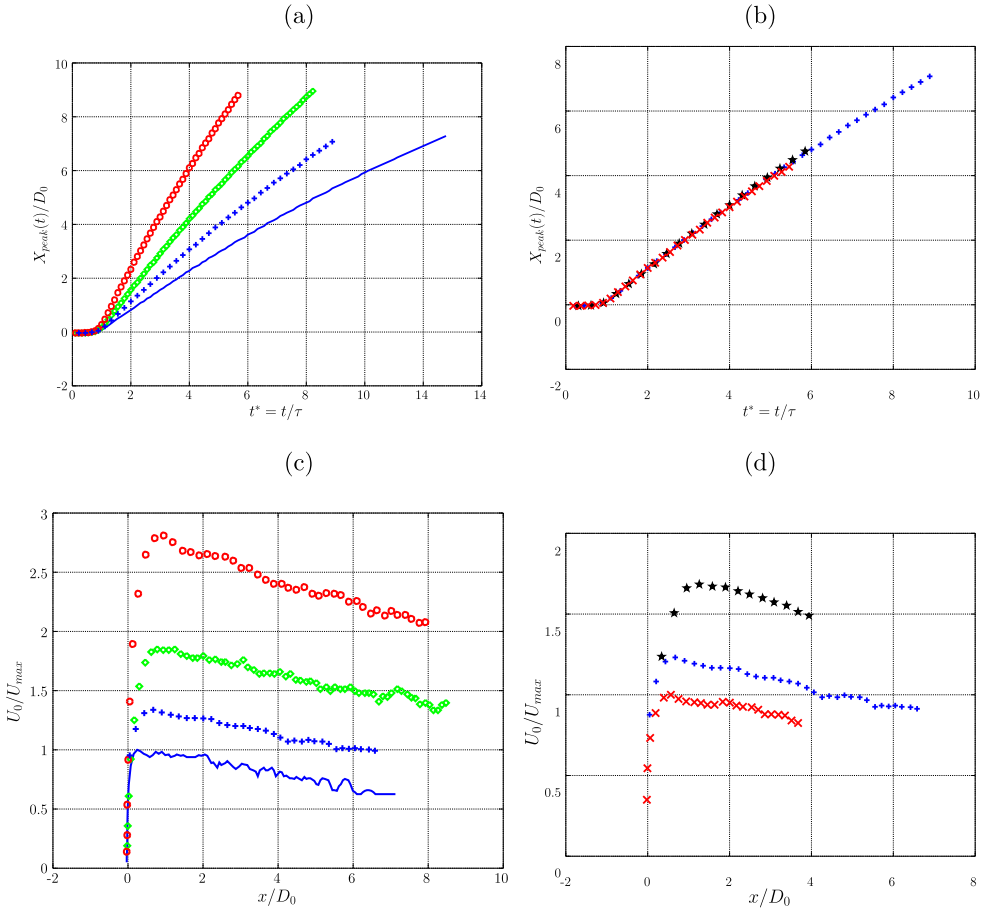

Figure 12. Ring properties. (a), (b) Axial ring position and (c), (d) ring self-induced velocity. The values were taken for different piston stroke with constant rise time $\tau = 18.1$ ms : $d_0 = 0.8$ mm (○), $d_0 = 0.6$ mm (◇), $d_0 = 0.48$ mm, (+), $d_0 = 0.4$ mm (−) and different rise time with constant stroke $d_0 = 0.48$ mm: $\tau = 13.0$ ms (⋆), $\tau = 18.1$ ms (+) and $\tau = 22.0$ ms (×). The corresponding maximum velocity $U_{\max}$ is found at minimum stroke in (c) and maximum rise time in (d).

ring (Hernández *et al* 2006). Even though it is interesting to see that a fairly good curve collapse can be obtained with the right choice of dimensionless variables, the dimensionless time scale is $t^* = t/\tau$ and the dimensionless axial position $\overline{X}_{\text{peak}}(t^*)$ is defined as

$$\overline{X}_{\text{peak}}(t^*) = \frac{X_{\text{peak}}(t^*)}{D_0}\left(\frac{d}{e}\right)^{\alpha} \tag{7}$$

In figure 13 we observe a good data collapse with an exponent $\alpha = -1.5$ for those rings created with different piston stroke, while the characteristic time scale τ makes its own with those rings created with a different rising time. The dimensionless self-induced velocity $\overline{U_0}$ is written accordingly as

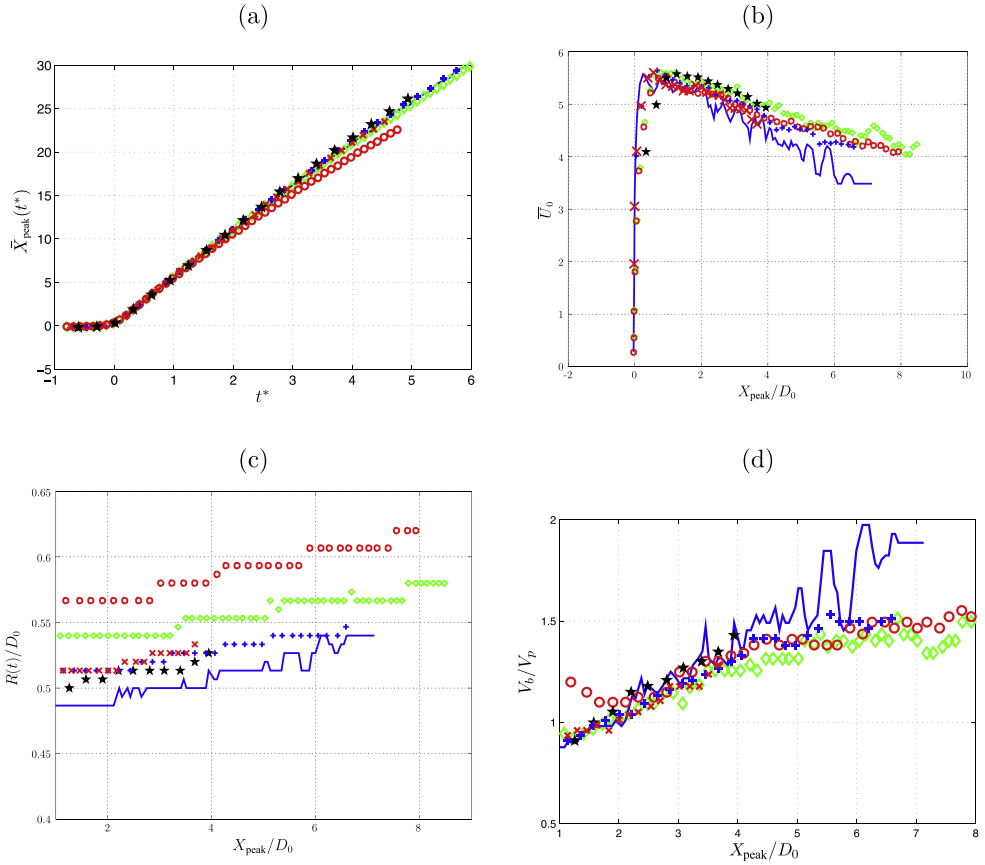

Figure 13. Temporal evolution of (a) dimensionless ring position $\overline{X}_{\text{peak}}(t^*)$, (b) dimensionless self-induced velocity, (c) ring radii and (d) ring bubble volume for the following the combination of piston stroke and rise time : (○) $d_0 = 0.8$ mm $-$ $\tau = 18.1$, (◇) $d_0 = 0.6$ mm $-$ $\tau = 18.1$, (+) $d_0 = 0.48$ mm $-$ $\tau = 18.1$, (–) $d_0 = 0.4$ mm $-$ $\tau = 18.1$ ms, (⋆) $d_0 = 0.48$ mm $-$ $\tau = 13$ and (×) $d_0 = 0.48$ mm $-$ $\tau = 22$ ms.

$$\overline{U}_0(t) = \frac{U_0(t)}{D_0}\left(\frac{d}{e}\right)^{\alpha}\tau \tag{8}$$

In figure 13(b) we plot the normalised values of the ring position and self-induced velocity where we get a consistent data collapse. As the ring moves forward we observe a slow increase in its radius $R(t)$ along the x-axis shown in figure 13(c). Because of data size issues, we only recorded some flow time steps to compute the ring radius. The piecewise evolution appears as a result of padding with the last vortex ring diameter until a new measurement is performed even though it seems that the positive slope of the curves does not depend on the method we adopted to create the ring (piston stroke or rising time). Nevertheless, the limited increase in diameter represents an important increase in the volume of the Kelvin oval as shown in figure 13(c).

The evolution of the ring's bubble volume V_b as fraction of the piston stroke volume (V_p) is naturally expected for rings moving at different Reynolds numbers. A linear increase of the bubble volume with the volume of the piston stroke is observed and the ratio $V_b/V_p = 1$ when the ring is about two nozzle diameters downstream.

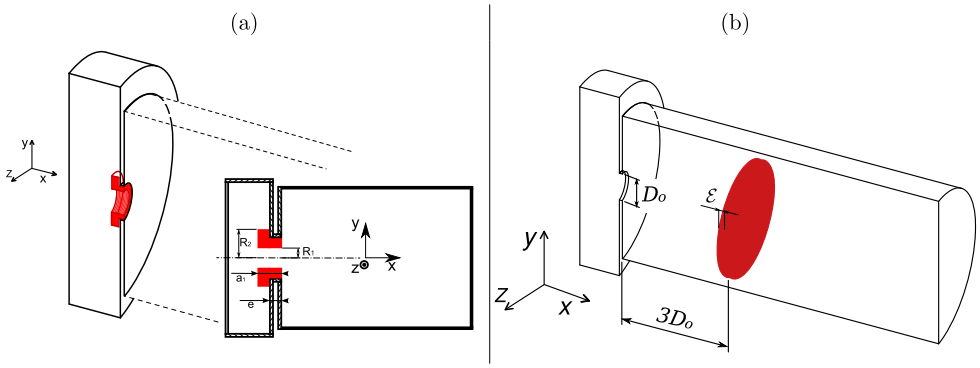

Figure 14. (a) Case A: the passive scalar is uniformly distributed in a ring at the nozzle border. (b) Case B: the scalar variable is uniformly distributed in a disk of diameter D_c and thickness e at $x = 3D_0$ from the chamber exit.

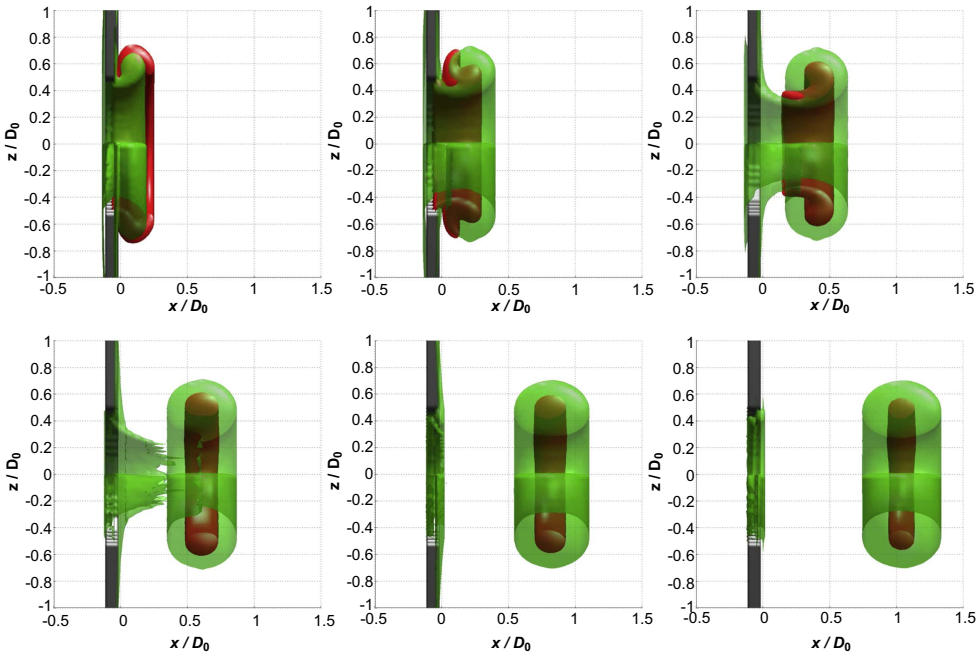

Figure 15. Case A: snapshots time sequence ($\Delta t = 0.005$ s between images) of a passive scalar isosurface (■) evolving inside the vortex ring at $Re = 700$, which is shown in the form of an isosurface of vorticity $\omega = 200$ s^{-1} (■). The passive scalar initial distribution corresponds to a uniform scalar, $C = 1$ in the borders of the nozzle wall. The isosurface shown (■) corresponds to a scalar value of $C = 0.05$ in order to display an outmost boundary of the scalar region inside the ring.

3.2. Two scalar distributions

In order to understand the ability of one single ring to transport a particular distribution of a scalar substance, we have considered two different initial scalar distributions in relation to the ring formation process. The first case (A) shown in figure 14(a) corresponds to an initial

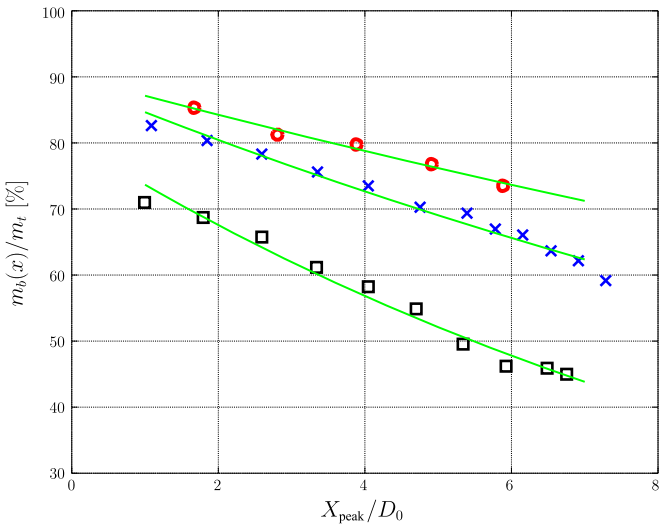

Figure 16. Case A: relative scalar mass m_b/m_t in the bubble as a function of the ring axial position for different piston strokes. $Re \sim 500$ (□), $Re \sim 950$, (×), $Re \sim 1400$ (○).

scalar distributed in the borders of the nozzle according to the following (arbitrary) dimensions: $R_1 = 4e$, $R_2 = 6e$ and $a_1 = 2e$ where $e = 1.5$ mm corresponds to the thickness of the nozzle. Rings were simulated with different Reynolds numbers, varying the piston stroke, to determine how much scalar mass can be picked up by the rings. The second case (B) shown in figure 14(b) corresponds to an initial disk-like scalar distribution of thickness ϵ and diameter $D_\epsilon/D_0 = 2.4$. Different cases varying ϵ were studied keeping the disk diameter D_ϵ constant and always smaller than the domain limits and was placed at $3D_0$ from the nozzle exit.

$$C(x, y, z, 0) = \begin{cases} 1 & \text{if } (3D_0 < x < 3D_0 + \epsilon) \ \wedge \ (y^2 + z^2) \leqslant D_\epsilon^2/4 \\ 0 & \text{otherwise} \end{cases} \tag{9}$$

3.2.1. Passive scalar in Case A. In this case the scalar is trapped by the ring during the formation process mediated by the rolling up of the vorticity sheets at the nozzle exit. Figure 15 displays this formation process and the entrainment mechanism when the initial scalar distribution is placed at the nozzle wall (figure 14(a)). The green sheet corresponds to an isosurface of vorticity and the red isosurface is the scalar. While this case is difficult to perform in a real experiment, it is very informative of this particular process. A complete entrainment of the scalar mass into the ring occurs shortly before the ring pinch-off, then the scalar isosurface changes in size with the axial distance indicating that some scalar mass is being lost from the bubble.

Once the ring moves away from the nozzle exit, the initial scalar mass is almost entirely swept away by the ring. It seems reasonable that the net scalar mass swept from the nozzle and then transported with the ring will benefit from higher piston strokes, because of the natural increase in the local shear at the nozzle but also in the bubble size.

The idea that increasing the piston stroke d_0 could increase the scalar mass trapped in the ring has been studied here varying the piston stroke. However, we must remember that the

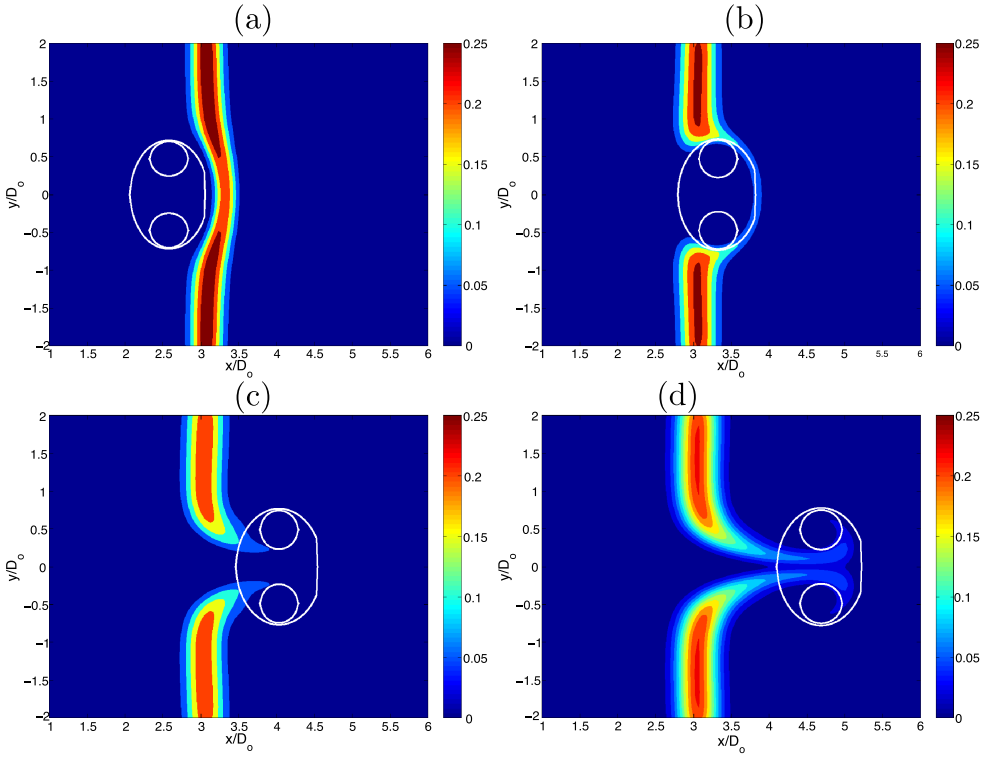

Figure 17. Case B: midplane sequence of the scalar entrainment by a ring crossing the scalar disk-like layer of $C = 1$ and thickness $\epsilon = D_0/3$, as a function of time or equivalent axial position. (a) $X_{\text{peak}}/D_0 = 2.6$. (b) $X_{\text{peak}}/D_0 = 3.0$, (c)$X_{\text{peak}}/D_0 = 4.0$ and (d) $X_{\text{peak}}/D_0 = 4.7$. The white lines correspond to the vortex ring bubble and the white circles the approximate region encircling the vortex core. The contour scale displayed has been limited to observe the scalar mass inside the ring.

higher the piston stroke the bigger the volume of the fluid discharge across the nozzle and the leading ring formed can be followed by a trailing jet (Gharib *et al* 1998) and therefore the possibility of an unwanted shedding of the scalar into the wake will potentially occur. In such cases, molecular diffusion will tend to spread the scalar into the ring wake while moving forward.

In contrast, short stroke ratios produce a very clean process as the molecular diffusion of the scalar from the inside of the ring bubble occurs over a time scale much larger than the time scale of the ring, therefore we see a relatively constant scalar loss rate in the linear decay of m_b shown in figure 16, normalised by the total scalar mass at $t = 0$ in the numerical domain, m_t. The linear fit of figure 16 corresponds to scalar mass values at spatial locations X_{peak}/D_0 where the ring bubble is well defined, i.e. after pinch-off. As the bubble definition relies on the finding of the zero velocity stagnation point in both the leading and trailing edge of the ring, if we perform this operation before pinch-off, this may lead to an unrealistic bubble size estimation. In the same figure we also note that the relative scalar mass inside the ring bubble increases with the ring's Reynolds number which is determined by the piston stroke. An increase in the piston stroke directly produces an increase of the mean velocity at the nozzle

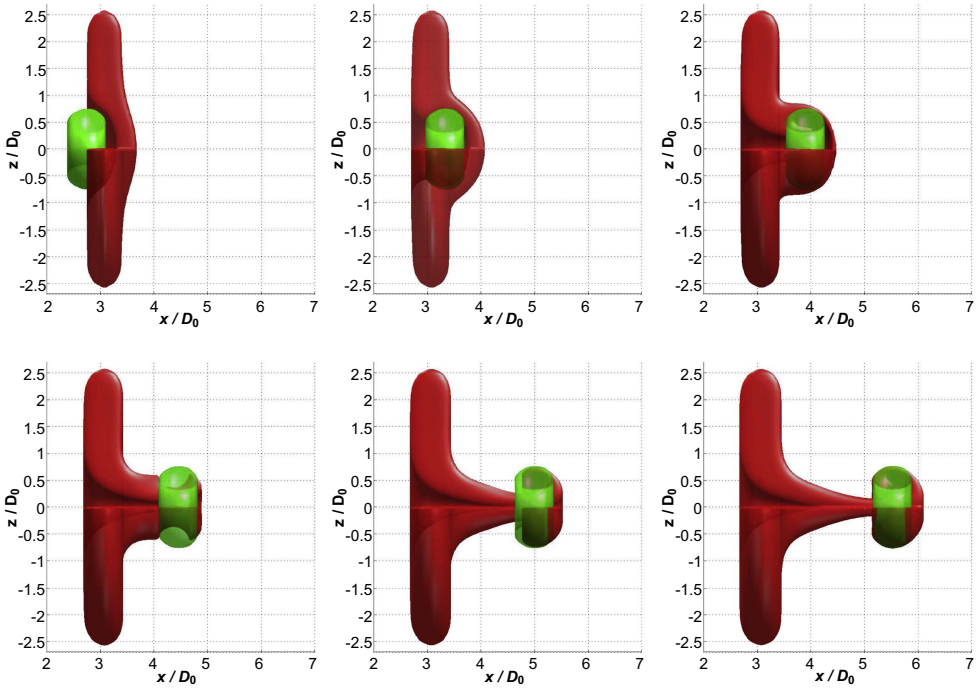

Figure 18. Case B: sequence of snapshots ($\Delta t = 0.005$ s between images) showing the time evolution of one isosurface of vorticity of the vortex ring $\omega = 200$ s^{-1} (■) interacting with a passive scalar isosurface disk-like distribution of initial thickness $\epsilon = D_0/3$ ($C = 0.05$, ■).

exit. This implies stronger transverse spatial gradients and therefore the high shear stress at the nozzle wall, precisely on the zone the scalar has been initially deposited.

3.2.2. Passive scalar in Case B. In this case the initial scalar is distributed in a disk placed at $3D_0$ downstream the nozzle exit. The use of this kind of barrier placed in the ring path has been reported in the literature using particle distributions instead of scalars (Uchiyama and Yagami 2008). In figure 17 we display a time sequence of the ring moving across the disk-like scalar layer of thickness $\epsilon = D_0/3$. At first the ring pushes the scalar layer forward creating an opening between the upstream and downstream regions. The forward effect is the result of the local advection of the layer by the upstream ring flow. However, the ring circulation will trap a thin scalar sheet which is ultimately entrained into the ring bubble. The faster the ring motion the higher the scalar mass incorporated into the ring bubble. This pushing-effect has been reported during the initial steps in the interaction between the rings and the distributions of small particles (Uchiyama and Yagami 2008).

The amount of trapped scalar is obtained by computing the scalar mass inside the bubble and the mass fraction that fills the ring core. We have performed different runs changing first the thickness of the disk-like scalar distribution, $\epsilon/D_0 = 0.13,\ 1/3,\ 2/3$ and then we have changed the piston stroke ratio d_0/D_0 for d_0= 0.4, 0.6 and 0.8 mm providing runs at different Reynolds numbers.

In the 3D plot shown in figure 18 we observe the interaction of the ring with a disk-like scalar distribution of thickness $\epsilon/D \sim 1/3$. Here we can identify two different stages; at first

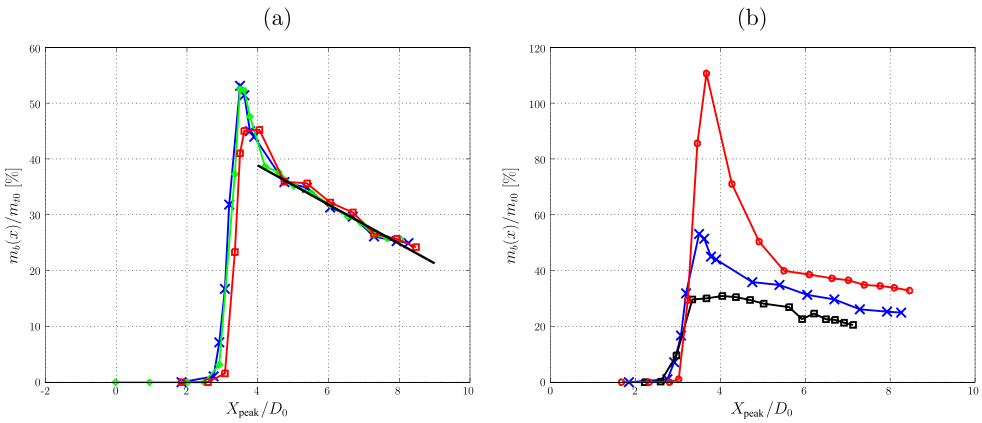

Figure 19. Case B. Scalar mass inside the ring bubble. (a) Different thickness ϵ at $Re = 700 : \epsilon/D_0 = 2/3$ (■), $\epsilon/D_0 = 1/3$ (◇) and $\epsilon/D_0 = 0.13$ (×). (b) Constant thickness $\epsilon/D_0 = 1/3$ and rise time $\tau = 18.1$ ms with different piston stroke: $d_0 = 0.8$ mm $- Re = 1430$ (●), $d_0 = 0.6$ mm $- Re = 950$ (×), $d_0 = 0.4$ mm $- Re = 530$ (■).

the scalar thickness show a little bit of spreading due to diffusion at the time the ring comes into contact with the disk. After that, the mechanism is governed by advection as the characteristic diffusive time scale (ϵ^2/Γ_c) is greater than the convective time scale (ϵ/U_0). After the first contact between the ring and the scalar disk, the ring starts to push the scalar radially and forward creating a scalar envelope which is then rolled up by the ring getting into the ring bubble and ring core.

The efficiency of a single ring to capture and convey a given scalar mass is presented on figure 19. We display the scalar mass fraction inside the ring bubble for both different Reynolds numbers Re and different thickness ϵ of the initial scalar distribution as a function of the axial position of the ring. In figure 19(a), when we keep the Reynolds number constant, the relative trapped scalar mass $m_b(x)/m_{t0}$ is relatively high and independent of the barrier thickness ϵ. There are however some differences on the first rising part of the curves and on the height of the overshoot. After that, it is observed an almost linear decay starting at $X_{\text{peak}}/D_0 = 4$.

The reference scalar mass used here, m_{t0}, is the mass contained in a disk-like volume of diameter $D_0 < D_\epsilon$ and thickness ϵ which correspond to the scalar barrier volume seen by the ring upon contact. This scalar mass is computed just before the ring makes contact with the barrier to take into account molecular diffusion during the ring's flight. As this reference value is smaller than the total initial scalar mass m_t in the disk-like barrier, the relative mass $m_b(x)/m_{t0}$ may be greater than unity.

The ring efficiency conveying the scalar out from the barrier may be higher if we increase the Reynolds number.

In figure 19(b) we display the influence of the Reynolds number of the ring on the scalar mass trapped inside the ring bubble. The shape of the curve is similar to the previous case but the time instants the ring make contact with the scalar distribution are different because of the Reynolds number. However if we consider the axial position of the ring, X_{peak}, we can align the curves with a common rising point followed by a different overshoot. The process also displays slightly different overshoot positions when the ring moves across the scalar barrier. The ring pushes the scalar barrier increasing the local concentration close to the front stagnation point which explain the overshoot. Faster rings push the barrier further

downstream increasing the amount of trapped scalar mass inside the bubble and producing therefore higher overshoots. This effect is illustrated in figure 17(b). The local increase of scalar concentration observed at the front of the ring is considered to belong to the ring bubble which explains the overshoot effect. After the ring breaks the barrier we observe a pinch-off process on the scalar as the ring moves downstream. As the convective time scale dominates the process across the barrier, the scalar loss rate (the slope just after overshoot on figure 19) may be explained mainly by the scalar shedding into the ring wake resulting from the pinch-off process.

If we focus on the scalar mass values computed at $X_{\text{peak}} > 5D_0$ (figure 17(d)), i.e. the bubble being a couple of diameters apart from the scalar barrier, we observe that the curve slopes on figure 19(b) become very similar. At this point the process displays a self-similar sustained scalar mass loss which may be explained by the combined action of molecular diffusion and scalar shedding, as it may occur with the vorticity of the ring (Maxworthy 1972).

4. Conclusions

We have studied the dynamics of a passive conserved scalar quantity entrained and then trapped by a self-propelling laminar and viscous vortex ring. With the aid of numerical simulations, vortex rings were studied during their most fundamental stages: the formation stage, the pinch-off and the asymptotic laminar state. The numerical simulation included the modelling of the vortex generator; piston, nozzle and chamber, in order to mimic as close as possible a real experiment. The simulation allowed us to control accurately the stroke ratio as well as the speed of the piston. Part of the numerical results were compared and validated with recent experimental records. The transport and mixing process of the passive scalar variable was studied numerically considering two initial scalar distributions: (i) the scalar substance was introduced into the ring during its formation, further focusing in the shedding into the wake of the ring; (ii) a disk-like scalar layer is placed in the ring's path in order to study the entrainment of the scalar substance into the ring as a function of both ring velocity and scalar thickness. In both cases, the scalar mass trapped inside the vortex bubble displays a pinch-off effect, followed by a sustained scalar loss attributed to the action of molecular diffusion. In case (ii) it was shown that the entrained scalar mass increases with both the Reynolds number and the thickness of the scalar layer in the propagation direction. However, proper normalisation of the scalar mass and time axis indicate a similarity only in the case of different scalar thickness. The ring can be viewed as a mechanism for scalar transportation along important distances showing however a constant scalar loss associated to the unavoidable action of both molecular diffusion and shedding into the ring's wake.

Acknowledgements

We are grateful to G Arérvalo for providing the experimental data. This work was partially supported by Fondecyt Grant No. 1085020.

References

Arévalo G, Hernández R H, Nicot C and Plaza F 2007 Vortex ring head-on collision with a heated vertical plate *Phys. Fluids* **19** 083603

Arévalo G, Hernández R H, Nicot C and Plaza F 2010 Particle image velocimetry measurements of vortex rings head-on collision with a heated vertical plate *Phys. Fluids* **22** 053604
Astudillo J 2008 Numerical simulation of the 3D impact of multiple vortex rings *Mechanical Engineering thesis* www.tesis.uchile.cl/tesis/uchile/2008/astudillo_jc/html/index-frames.html
Chatelain P, Kivotides D and Leonard A 2003 Reconnection of colliding vortex rings *Phys. Rev. Lett.* **90** 054501-1
CRC Handbook of Chemistry and Physics, 2009
Dabiri J and Gharib M 2004 Fluid entrainment by isolated vortex rings *J. Fluid Mech.* **511** 311–31
FLUENT INC. Fluent 6.3: Tutorial Guide. 2005
Gharib M, Rambod E and Shariff K 1998 A universal time scale for vortex ring formation *J. Fluid Mech.* **360** 121–40
Glezer A 1988 The formation of vortex rings *Phys. Fluids* **31** 3532–42
Glezer A and Coles D 1990 An experimental study of a turbulent vortex ring *J. Fluid Mech.* **211** 243–83
Hernández R H, Cibert B and Béchet C 2006 Experiments with vortex rings in air *Europhysics Lett.* **75** 743–9
Hernández R H and Monsalve E 2015 Experimental observation of the collision of three vortex rings *Fluid Dyn. Res.* **47** 035513
Hicks W M 1885 Researches on the theory of vortex rings—part II *Philosophical Transactions of the Royal Soc. London* A **176** 725–80
James S and Madnia K 1995 Direct numerical simulation of a laminar vortex ring *Phys. Fluids* **8** 2400–14
Jang D S, Jetli R and Acharya S 1986 Comparison of the PISO, SIMPLER and SIMPLEC algorithms for de treatment of the pressure-velocity coupling in steady flow problems *Numer. Heat Transfer* **10** 209–28
Kelvin L 1867 The translatory velocity of a circular vortex ring *Phil. Mag.* **33** 511–2
Kelvin L 1881 On the average pressure due to impulse of vortex rings on a solid *Collected Works* **4** 188
Lamb H 1932 *Hydrodynamics* 6th edn (Cambridge, UK: Cambridge University Press)
Linden P F and Turner J S 2001 The formation of 'optimal' vortex rings, and the efficiency of propulsion devices *J. Fluid Mech.* **427** 61–72
Maxworthy T 1972 The structure and stability of vortex rings *J. Fluid Mech.* **51** 15–32 part 1
Maxworthy T 1977 Some experimental studies of vortex rings *J. Fluid Mech.* **81** 465–95
Mohseni K, Ran H and Colonius T 2001 Numerical experiments on vortex ring formation *J. Fluid Mech.* **430** 267–82
Muller E A and Didden N 1980 Zur erzeugung der zirkulation bei der bildung eines ringwirbels an einer dusenmundung *Stroj. Casop.* **31** 363372
Patankar S V 1980 Numerical heat transfer and fluid flow. *Series in Computational Methods in Mechanics and Thermal Science* (United States: Taylor & Francis)
Roberts P H and Donelly R J 1970 Dynamics of vortex rings *Phys. Lett.* A **31** 137–8
Saffman P G 1970 The velocity of viscous vortex rings *Stud. Appl. Math.* **49** 371–80
Sau R and Mahesh K 2007 Passive scalar mixing in vortex rings *J. Fluid Mech.* **582** 449–61
Shariff K and Leonard A 1992 Vortex rings *Annu. Rev. Fluid Mech.* **24** 235–79
Southerland K, Porter J R, Dahm W J A and Buch K B 1991 An experimental study of the molecular mixing process in an axisymmetric laminar vortex ring *Phys. Fluids* A **3** 1385–92
Uchiyama T and Yagami H 2008 Numerical simulation for the collision between a vortex ring and solid particles *Powder Technol.* **188** 7380
Uchiyama T and Yagami H 2009 Vortex simulation for non-axisymmetric collision of a vortex ring *Adv. Power Technology* **20** 447–54
Widnall S E and Sullivan J P 1973 On the stability of vortex rings *Proc. R. Soc. Lond.* A **332** 335–53